CCFE
CULHAM CENTRE FOR FUSION ENERGY

UK Atomic Energy Authority

UKAEA-CCFE-PR(25)338

Matthew J. Lloyd, Kan Ma, Andrew J. London,
James Gibson, Andy Watson, Chris Hardie,
Alexander Knowles

Formation of (Ti,W)Fe2 C14 Laves Phase in the W-Ti-Fe System and Impact on Mechanical Properties

Formation of (Ti,W)Fe2 C14 Laves Phase in the W-Ti-Fe System and Impact on Mechanical Properties

Matthew J. Lloyd, Kan Ma, Andrew J. London, James Gibson,
Andy Watson, Chris Hardie, Alexander Knowles

This is a preprint of a paper submitted for publication in
Journal of Alloys and Compounds

Formation of (Ti,W)Fe_2 C14 Laves Phase in the W-Ti-Fe System and Impact on Mechanical Properties

Matthew J. Lloyd [1,*], Kan Ma [1,4], Andrew J. London [2], James Gibson [2], Andy Watson [1,3], Chris Hardie [2], and Alexander Knowles [1,*]

1. School of Metallurgy and Materials, University of Birmingham, B15 2TT, United Kingdom
2. UK Atomic Energy Authority, Culham Campus, Oxfordshire OX14 3DB, United Kingdom
3. Hampton Thermodynamics Limited, Hampton, TW12 1NL, UK
4. Department of Mechanical Engineering, City University of Hong Kong, Kowloon, Hong Kong

*Corresponding authors: m.j.lloyd@bham.ac.uk & a.j.knowles@bham.ac.uk

Journal of Alloys and Compounds

ABSTRACT

Tungsten-based BCC superalloys utilising coherent intermetallic strengthening offer a route to improved high temperature strength. Recently proposed W-Ti-Fe alloys employ B2 TiFe phase in an A2 BCC matrix to achieve this strengthening, however, other phases such as the $TiFe_2$ Laves phase can form at higher temperatures. In this study the formation of a (Ti,W)Fe_2 C14 phase in a BCC W-rich matrix is observed in a W–16Ti–4Fe (at.%) alloy produced by vacuum arc-melting and were annealed at 1400°C. There was no evidence for the formation of either the TiFe B2 or W_6Fe_7 μ phase from analysis of the TEM diffraction patterns. The C14 Laves phase has a composition of 8.8±0.2W, 23.3±0.2Ti and 68.0±0.8Fe (at.%) consistent with (Ti,W)Fe_2, which formed a continuous region along the boundaries between the W-rich BCC prior-dendrites, as well as in smaller isolated precipitates. The prior dendritic regions consisted of W-rich BCC phase with a composition of 84.10±0.41W, 13.94±0.73Ti and 1.94±0.73Fe (at.%). Thermodynamics calculations using CALPHAD predicted the formation of a W rich BCC phase and a Ti and Fe rich liquid phase initially, which was not consistent with experimental findings. A revised calculation which reduced the stability of the μ phase at high temperatures led to an improved prediction, consistent with our experimental results. To investigate the mechanical impact of the C14 phase a combination of continuous stiffness measurement nanoindentation and high-speed nanoindentation mapping was used to study the mechanical properties of the matrix and precipitate phases, which showed that the C14 phase exhibits a very high hardness relative to the W-rich matrix phase. An average nanohardness of 6.68±0.02 GPa was measured at depth of X using continuous stiffness nanoindentation, which is higher than comparable B2 reinforced WTiFe alloys. These findings confirm the ability of the $TiFe_2$ phase to induce hardening in W-Ti-Fe alloys.

INTRODUCTION

Tungsten-based BCC-superalloys have recently been proposed as a route to improved high-temperature strength via the formation of coherent ordered-BCC B2 phase precipitates. The design principle behind these alloys is analogous to the ordered-FCC ɣ' phase found in FCC Ni-based superalloys. The formation of a β(BCC)-β'(B2) two-phase microstructure has been demonstrated in many BCC systems [1–6]. In the W-Ti-Fe system, B2 TiFe precipitates were produced during heat treatment at 1250°C [1,2], however this system has seen only limited study and there are uncertainties as to the phase stability and properties for W rich W-Ti-Fe compositions. Alloys based on the principles demonstrated in these studies have the potential for extreme applications including advanced nuclear reactors and aerospace.

Nuclear fusion is an area in which the principle of intermetallic strengthening could offer a further advantage over just high-temperature strengthening. Radiation-induced embrittlement remains a critical issue for W under neutron irradiation [7–9] and requires improvement if fusion energy is to be commercially viable. Radiation-resistant materials are designed using the formation of a high density of point defect sinks, which can absorb excess point defects induced in displacement cascades, thus limiting embrittlement from the formation of extended defects. Typical approaches to this include the dispersion of oxide particles (e.g. Oxide Dispersion Strengthened (ODS) steels and ODS W [10,11]), the formation of nanocrystalline grains (e.g. Ultra-Fine Grained (UFG) W [12–14]) and fine-scale carbide formation (e.g. Castable Nanostructured Alloy (CNA) Steels [15] and TiC/W_2C/ZrC dispersion strengthened W [16–19]). Embedded nano-scale intermetallic phases could offer a similar route to reducing excess point defect concentrations [20], using only heat treatment to induce their formation, however more work is needed to address the poor ductility of the matrix phase in current fusion compatible alloys. Beyond fusion, Ti-based C14 phases are also under investigation as candidate materials for hydrogen storage, necessitating a greater understanding of their mechanical properties. Alloys consisting of a Fe_2(Ti,Mo) matrix reinforced by A2 T/Mo have been demonstrated as a candidate high strength alloy with improved toughness [21].

The interactions between W and alloying additions are not well understood, leading to poorly characterised ternary phase diagrams for W-rich compositions. This limits the ability of predictive models such as CALPHAD-based methods [22,23] to predict the solubility limits and solvus positions with temperature. In addition to the desired B2 phase, the formation of several other intermetallic compounds is possible, depending on the alloy composition and heat treatments used. For the W-Ti-Fe system, the formation of a liquid phase at temperatures below 1400 °C and a $TiFe_2$ C14 Laves phase during heat treatments can be problematic for alloy development. There is scarce information on the behaviour of the $TiFe_2$ C14 Laves phase in this system, particularly its effect on mechanical properties and the boundaries of the multi-phase regions between the BCC and C14. Laves phases are generally observed to exhibit poor mechanical properties and are typically brittle at room temperature [24,25]. C14-phase $ZrFe_2$ and $ZrMn_2$ in Ti-based alloys have been shown to strongly limit dislocation motion and exhibit a high hardness [26]. Laves phases have also been utilised in novel maraging steels [27] and Cr alloys [28]. There is very little information on the mechanical properties of the $TiFe_2$ phase specifically, and its influence when embedded in a BCC matrix phase.

This study aims to provide new insights into the formation and mechanical properties of the $TiFe_2$ C14 phase using heat treatments within the W-Ti-Fe system, to aid onward optimisation work and better understand the implications of forming this phase during processing. This study focusses on the W rich corner of the ternary phase diagram to investigate the regions between the BCC solid solution and the Fe rich C14 phase.

METHODOLOGY

To investigate the phases that form in the W-Ti-Fe ternary system, thermodynamic calculations were performed using the thermodynamic description for the ternary W-Ti-Fe system taken from [2]. Figure 1 shows an isothermal section of the ternary W-Ti-Fe phase diagram at 1400°C, alongside binary phase diagrams for the W-Ti, Fe-Ti and W-Fe systems as calculated using this ternary database with ThermoCalc. In the Ti-Fe binary system, both B2 TiFe and C14 $TiFe_2$ phases are present between room temperature and the melting temperature of the

alloy. At 1400°C the B2 phase is dissolved into the liquid phase whereas the $TiFe_2$ phase remains stable at this temperature, though close to the liquidus line.

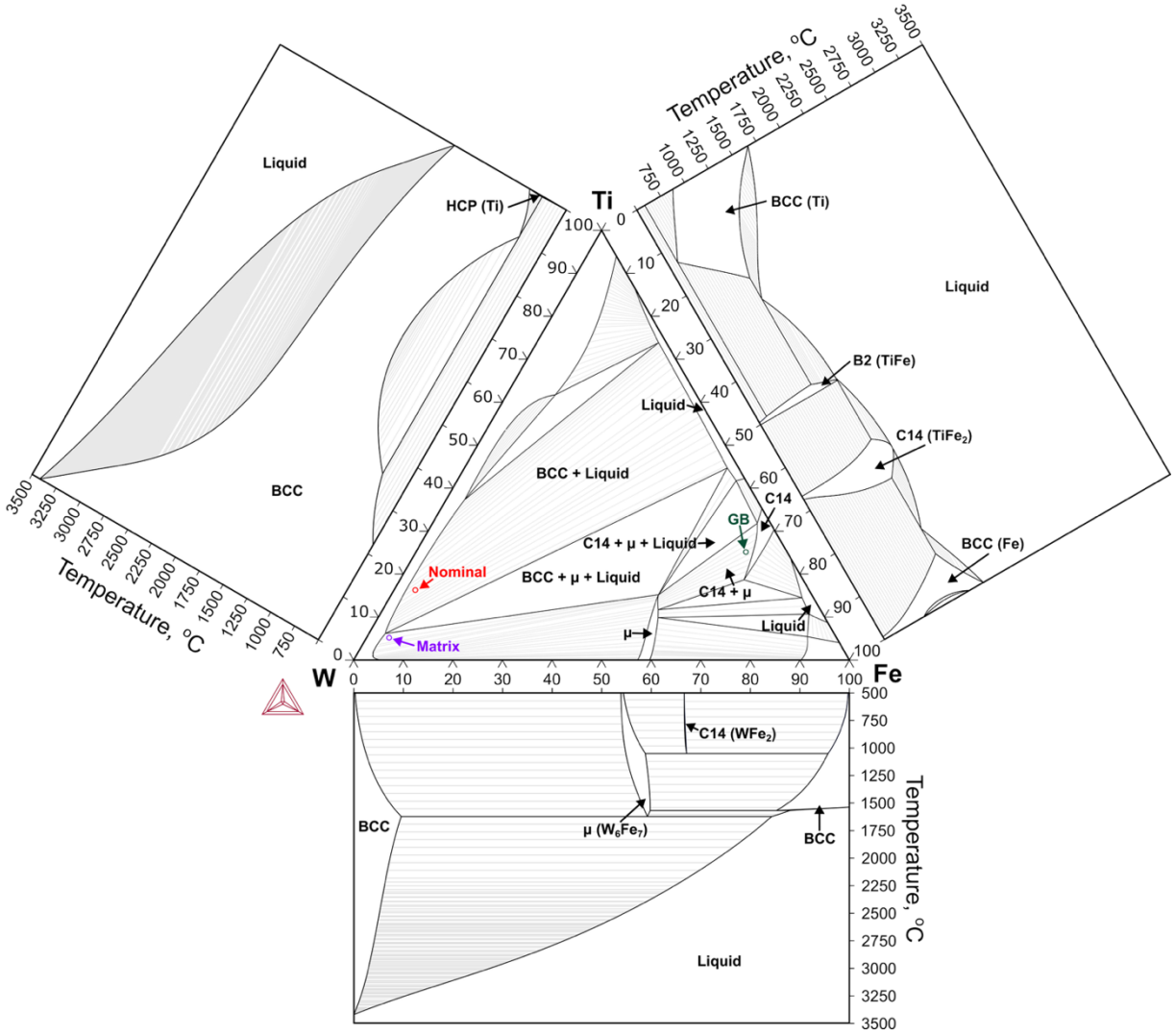

Figure 1: Isothermal section of W-Ti-Fe phase diagram at 1400°C calculated using ThermoCalc, alongside binary W-Ti, Ti-Fe and W-Fe phase diagrams. Concentrations are given in at.%. Constructed using the TCTI3 Ti-alloys database.

A composition of W-16Ti-4Fe at.%, (W-4.88Ti-1.42 wt.%) was chosen for investigation. The position of this nominal composition is highlighted in the ternary phase diagram shown in Figure 1, and lies within the dual-phase BCC and liquid region. An ingot of the alloy was produced by ACI alloys using vacuum arc melting. A section of the ingot was annealed for 72 hours at 1400 ˚C using a Carbolite tube furnace with a flowing mixture of Ar+5%H to prevent oxidation. After the 72 hour hold at 1400 °C, the specimen was furnace cooled inside the furnace until it reached room temperature. After annealing, the ingot was sectioned into 1.5 mm thick slices using wire-fed Electric Discharge Machining (EDM) and ground using successively finer grit abrasive paper to 2500 grit, followed by polishing with 3um and 1um diamond suspension and OPS colloidal silica solution. Scanning electron microscopy (SEM) Secondary Electron (SE)/Backscattered Electron (BSE) imaging and elemental analysis with

Energy-Dispersive Spectroscopy (EDS) was performed using a ThermoFisher Scientific Apreo 2S HiVac FEG-SEM

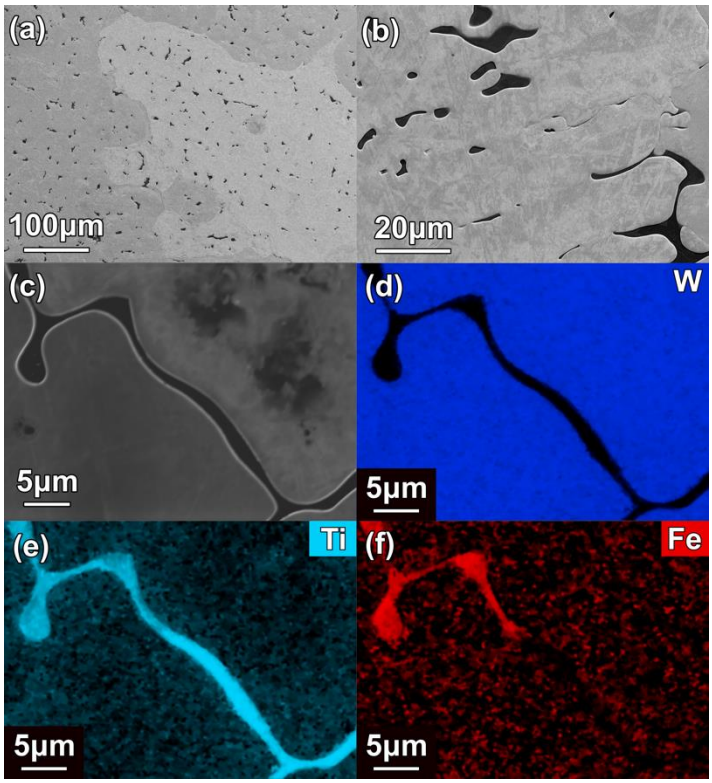

Figure 2: SEM Micrographs of the as cast specimen showing SE images in (a) and (b) and a BSE image in (c). (d) (e) and (f) show EDS maps of W, Ti and Fe respectively.

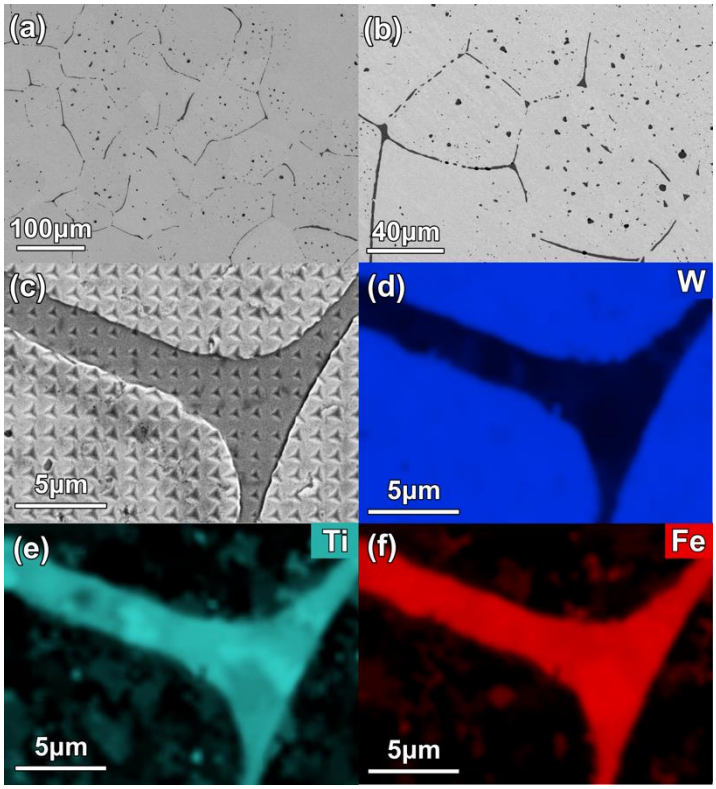

Figure 3: SEM Micrographs of the annealed specimen shown in BSE images (a) and (b), and SE imaging of an area onward analysed by nanoindentation mapping in (c). EDS maps of W, Ti and Fe are shown in (d), (e) and (f) respectively.

equipped with a ColorSEM UltraDry EDS detector and an FEI Quanta 3D FIB-SEM. EDS measurements were performed using an acceleration voltage of 10 kV. Mapping was performed using a resolution of 768x512, a current of 3.2 nA, a dwell time of 4us and a total acquisition time of 643 s.

EDS measurements of the various phases were performed using an average of 5-point spectra which used an acquisition time of 15s each, which resulted in between 100-275k counts per spectrum. Quantitative SEM-EDS mapping was performed using the Ti Kα (4.51 keV), Fe Kα (6.40 keV) and W Mα (1.78 keV) lines, using Axia ChemiSEM software. TEM foils were prepared from two regions of the specimen: 1) across the matrix/intermetallic interface and 2) in the centre of the BCC prior-dendrites. Foils were prepared using a FIB lift-out [29] using a FEI Quanta 3D dual-beam FIB-SEM. The microstructure and composition of the two phases in the foil were examined with TEM using an FEI Talos F200X TEM operated at 200 kV and processed using the Velox software package for elemental mapping and analysis. Diffraction patterns were acquired from the two phases and compared against a simulated diffraction pattern to confirm the crystal structure. The software, Singlediffract was used to simulate the selected area diffraction patterns using CIF files for the W and TiFe2 structures [ref] using default absorption factors provided by the software.

To examine the mechanical properties of the two phases the alloy was indented using a KLA iMicro Nanoindenter. The samples were mounted onto Al stubs using CrystalBond and indented at a strain rate of 0.2 s^{-1} using a Continuous Stiffness Measurement (CSM) method to enable the hardness and modulus to be measured as a function of depth, with a diamond Berkovich tip calibrated against fused silica [30,31]. An array of 5x5 indents were performed to a maximum final depth of 2 um. The hardness in these measurements was compared between depths of 1 and 1.5 µm to reduce indentation size effects [32]. Load-controlled rapid nanoindentation mapping was carried out using the "Nanoblitz 3D" method [33] using a target load of 4mN chosen to give an approximate depth of 150nm in the matrix. This depth is suitable to extract reliable hardness and modulus measurements, whilst preventing the overlap of individual indents using a spacing of 1.1 um (approximately 7 times the indentation depth). An array of 200 x 200 indents was used giving a total of 40,000 measurements over a 220 x 220 µm area to provide qualitative comparison of the two phases. Vickers microhardness (HV0.1) measurements were performed using a Beuhler DiaMet to 0.1 kilograms-force using a total of 10 indents with a spacing of 0.5 mm. Modified CALPHAD-based calculations were performed using Pandat and PanOptimiser. Based on the experimental examination, the relative stability of the W_6Fe_7 phase was adjusted using a temperature-dependent term.

Results and Discussion

Micrographs and EDS maps of the as-received specimen are shown in Figure 4. The specimen had large light contrast dendritic regions >100um in size, as well as a dispersion of dark contrast regions distributed heterogeneously across the cross section of the specimen. In addition to the small inclusions, some regions appeared to show formation of the secondary phase along the interdendritic boundaries, as shown in Figure 4(c). EDS scans of the small inclusions showed that these were primarily Ti and Fe-rich, with a composition of 5.8%W-73.3%Ti-1.0%Fe (at.%), as shown in Table 1. EDS mapping of the interdendritic boundary phase showed that these were also primarily Ti and Fe rich, though as shown in Figure 4 (d)-(f) there was incomplete mixing between Ti and Fe in this phase. The ratio of Ti and Fe in the precipitate phase is near the low-temperature eutectic mixture in the Ti-Fe phase diagram shown in Figure 1. The melting temperatures of pure Ti and Fe are at 1670 and 1536 °C, respectively, considerably lower than W at 3407 °C for W [34]. This large difference in melting point results in the initial solidification of the W phase during arc melting, followed by the Fe and Ti in the interdendritic regions. We therefore suggest that the Ti/Fe-rich inclusion in the as-cast is caused by the solidification of this remaining liquid phase during cooling in the manufacturing process and incomplete diffusion of these species into the W-rich dendrites.

SE images of the sample after annealing are presented in Figure 5 shows large dark contrast regions formed at the prior-interdendritic region of the sample. In addition, dark contrast features within the prior

dendrites correspond to 1-2 µm sized precipitates that have formed across a large area. The alloy has a coarse grain structure, with grains between 100 and 500 µm in size, consistent with the prior dendrite size from the as-cast sample. The bulk composition was measured using EDS over a low magnification area including the matrix, grain boundary and precipitates. The measured concentrations of W, Ti and Fe in at.% were 87.6 ± 0.3, 7.1 ± 0.2 and 5.2 ± 0.5, respectively.

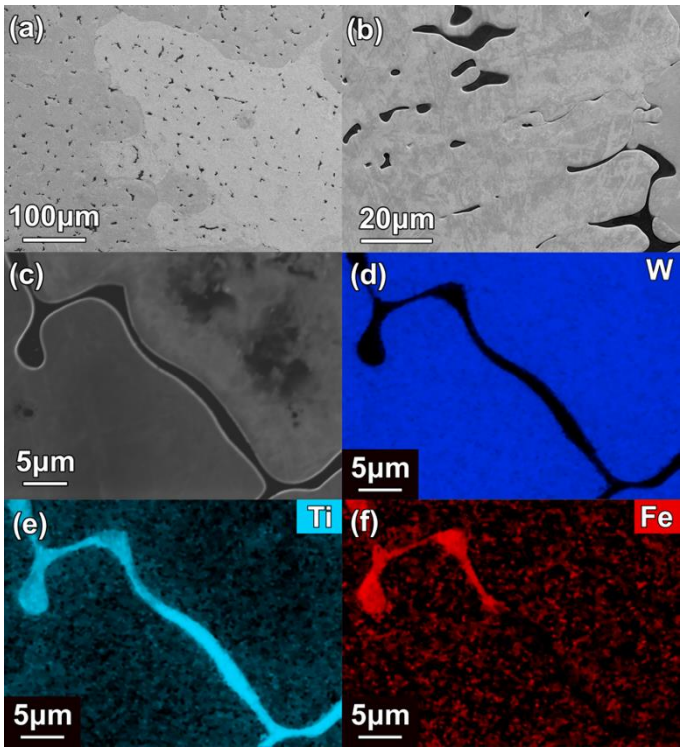

Figure 4: SEM Micrographs of the as cast specimen showing SE images in (a) and (b) and a BSE image in (c). (d) (e) and (f) show EDS maps of W, Ti and Fe respectively.

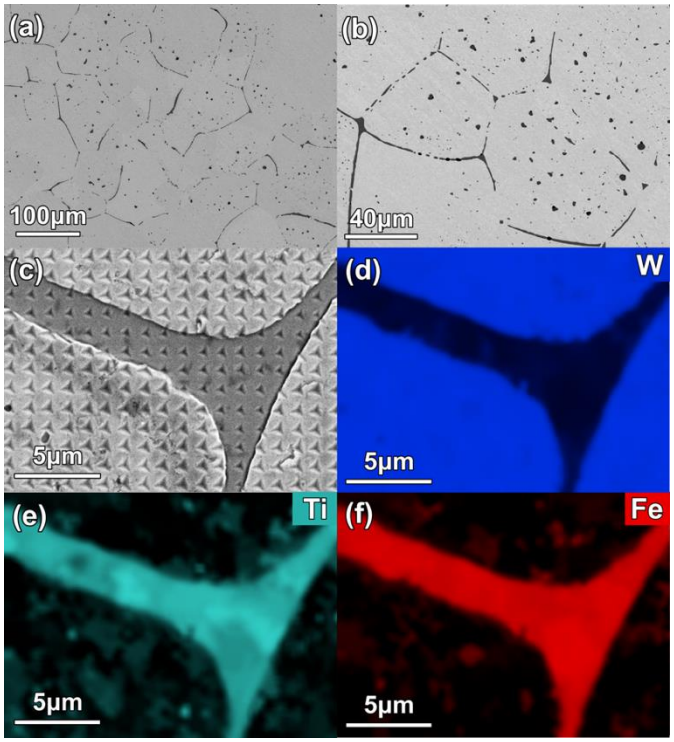

Figure 5: SEM Micrographs of the annealed specimen shown in BSE images (a) and (b), and SE imaging of an area onward analysed by nanoindentation mapping in (c). EDS maps of W, Ti and Fe are shown in (d), (e) and (f) respectively.

Table 1: Chemical composition of BCC matrix and intermetallic phases in as-cast and annealed samples measured using SEM-EDS. The uncertainty reported for each average value is the standard uncertainty, obtained by propagating the individual quantification uncertainties provided by the EDS software for each point spectrum.

Specimen	**Phase**	**W (at.%)**	**Ti (at.%)**	**Fe (at.%)**
As-Cast	Dendritic	84.1 ± 0.4	13.9 ± 0.7	1.9 ± 0.73
	Precipitates	5.8 ± 0.1	73.3 ± 0.7	21.0 ± 1.1
	Inter-dendritic (Ti-rich)	2.1 ± 0.1	97.4 ± 1.2	0.5 ± 0.4
	Inter-dendritic (Fe-rich)	1.0 ± 0.1	60.5 ± 0.8	38.5 ± 1.8
Annealed	Prior-dendritic	90.1 ± 0.2	5.5 ± 0.3	4.5 ± 0.7
	Precipitates	6.7 ± 0.1	25.6 ± 0.2	67.7 ± 0.7
	Prior-interdendritic	8.8 ± 0.2	23.3 ± 0.2	68.0 ± 0.8

EDS measurements of the various regions in the annealed sample are shown in Table 1, alongside the measurements from the as-cast sample. In the annealed sample, measurements were taken from the centres of the bright contrast grains, or prior dendritic region (approximately 4-5 µm away from the grain boundary phase, which showed no visible precipitates). These spectra gave a matrix composition of 90.1W, 5.5Ti and 4.5Fe (at.%), compared with 84.1W, 13.9Ti and 1.9Fe (at.%) for the as-received specimen. There is an apparent decrease in Ti and W, and an increase in Fe content based on these measurements; however, this is not reflected in an increase in Ti/W in any of the other phases. We therefore suggest that this is a result of macroscopic variation in

composition across different regions of the ingot, which is possible given the large differences in melting temperatures between the constituent elements.

Quantitative EDS measurements from the prior-interdendritic or grain boundary phase and precipitate phases (shown by dark contrast in Figure 5) showed that the composition was consistent across both regions. In the prior-interdendritic regions, the composition was measured to be 8.8W, 23.3Ti and 68.0Fe (at.%) respectively. Similarly, in the isolated precipitates, the composition was 6.7W, 25.6Ti and 67.7Fe (at.%). The ratio of Fe to Ti in both of these phases is consistent with the $TiFe_2$ C14 Laves phase, although the nominal composition of the sample lies within the A2 + Liquid region of the phase diagram shown in Figure 1. Also highlighted in Figure 1 is the measured composition of the prior-interdendritic (GB) and the prior-dendritic (matrix) regions of the sample, measured using EDS. This shows that the prior—dendritic region is within the A2 + W_6Fe_7 μ phase field, but close the boundary with the predicted A2, and A2 + μ + liquid regions. As the predictions did not suggest the formation of the C14 phase, the crystal structure of the prior-interdendritic and precipitate phases in the annealed material were examined using STEM and STEM-EDS.

High Angle Annular Dark Field (HAADF) images are shown in Figure 6(a), showing the region examined with TEM. The bright region shows the W-rich matrix or prior-dendritic phase. The dark regions correspond to the grain boundary/prior-interdendritic phase and smaller isolated precipitates which are distributed throughout the matrix. Selected area diffraction patterns confirm that the matrix phase has a A2 BCC structure, as shown in Figure 6(b). Superlattice spots corresponding to the TiFe B2 phase were not observed, and this phase is not predicted to be stable at 1400 ^{o}C, as shown in Figure 1. There was no indication that this phase formed upon furnace cooling from 1400^{o}C. Both the grain boundary phase and the isolated precipitates were confirmed to have a C14 structure as shown in Figure 6(c). The crystal structure of the precipitate phase was confirmed by comparing the diffraction spots shown in Figure 6(c) to a simulated diffraction pattern using a $TiFe_2$ Laves phase.

The lattice parameters obtained by the fit were a=b=4.7829 Å, c=7.9488 Å, α = β = 90°, γ = 120°. The values agree well with lattice parameters predicted for the $TiFe_2$ Laves phase using DFT (a=4.686 Å and c=7.732 Å) [35].

To investigate the phase composition, quantitative STEM-EDS maps of W, Fe and Ti were performed and are shown in Figure 6(d)-(f) with the corresponding concentration. For quantification, the K-lines were used for Ti and Fe, whereas the L-lines were used for W. As suggested by the SEM-EDS maps, the matrix consists mostly of W with a small concentration of dissolved Fe and Ti. STEM-EDS measurements show a matrix composition of 90.5 at.% W, 5.8 at.% Fe and 3.7 at.% Ti. The C14 phase consists mostly of Fe and Ti with only 6.9 at.% W. The

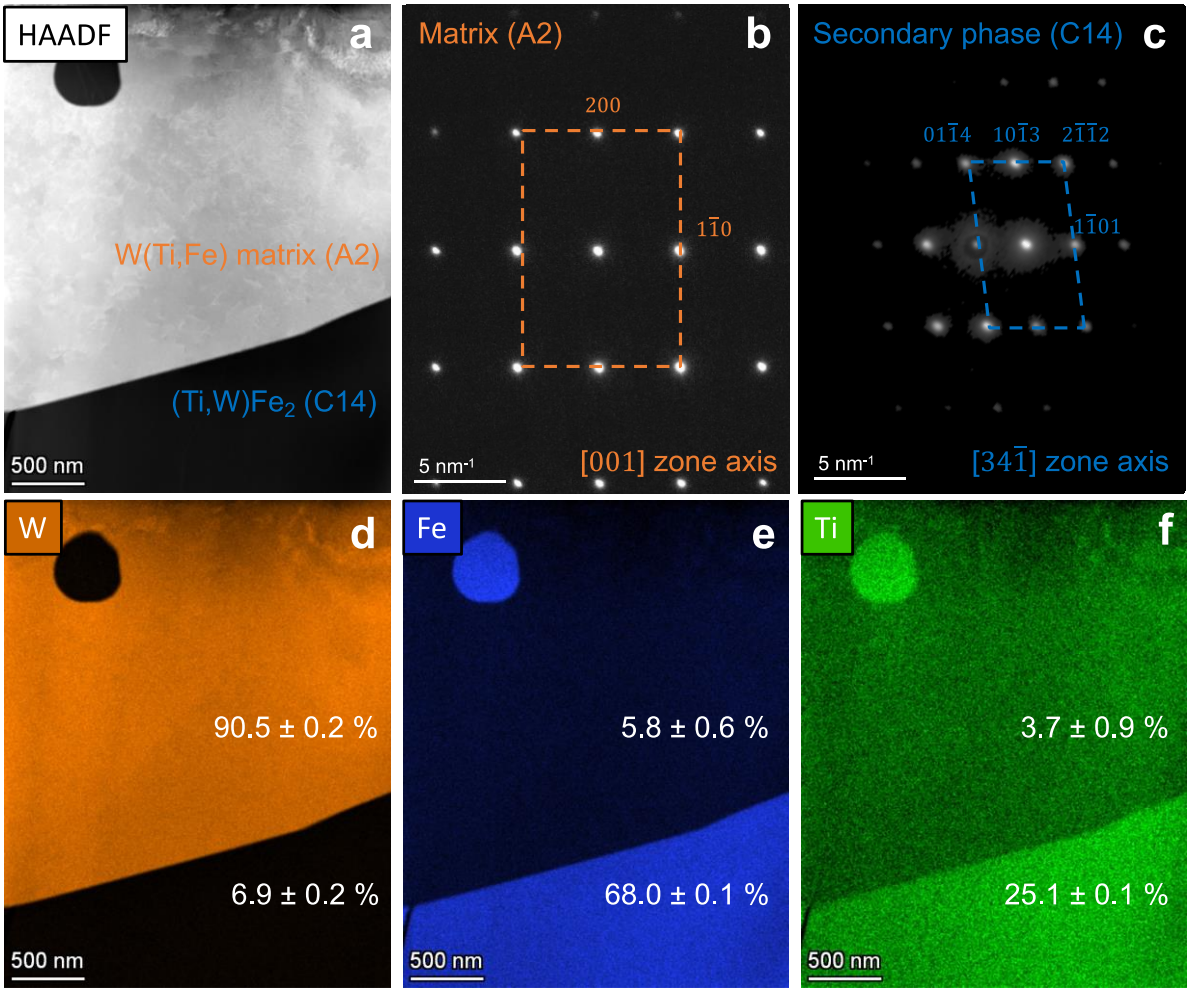

Figure 6: (a) HAADF image of BCC W(Ti,Fe) matrix and C14 (Ti,W)Fe2 phases with corresponding selected area diffraction patterns shown in (b) and (c). EDS maps of the same region showing the W, Fe and Ti concentration are shown in (d) (e) and (f) respectively.

ratio of Fe to (W,Ti) is 68.0 to 32.0, which is consistent with the stoichiometry of the $(W,Ti)Fe_2$ phase. The EDS

maps also show that the composition of the C14 phase is consistent between the isolated precipitates and the grain boundary phase.

It is possible that the B2 phase could form on cooling into fine-scale precipitates in the centre of the grains away from the Fe-rich C14 phase, as the nominal alloy composition is within the triple-phase A2 + C14 + B2 region at temperatures below 1400 ˚C (see Figure 1). As the alloy was cooled through this region during removal from the furnace, the possibility of B2 formation in the prior-dendritic region was investigated using a TEM lamella lifted out from the centre of a W-rich grain. Examination of this foil found no superlattice reflections in the diffraction pattern and no evidence of B2 precipitates. The composition measured with STEM-EDS was 5at.% Ti and 1at.% Fe, similar to the matrix phase observed adjacent to the C14 phase in Figure 5 but slightly depleted in Fe.

The nominal composition of the sample is predicted to be within the BCC + liquid region of the W-Ti-Fe ternary phase diagram at 1400 °C, Figure 1, which does not immediately explain the formation of the C14 Laves phase during heat treatment. Our findings suggest the existence of a two-phase A2 + C14 phase region between the measured prior-interdendritic and prior-dendritic compositions. SEM-EDS maps shown in Figure 4reveal that the as-cast microstructure consists of a W-rich BCC matrix phase intersected by grain boundaries decorated with the Ti and Fe alloying additions. These elements are not homogeneously distributed along the boundaries: some regions are nearly pure Ti, while others contain approximately 60% Ti and 40% Fe. This suggests that the grain boundary phases lie within or near the Ti/Fe-rich liquid region of the phase diagram (Figure 1), and likely formed during initial melting, due to the large differences in melting points between Ti/Fe and W.

Upon heating the specimen to 1400 ºC, Fe and Ti interdiffuse in the prior-interdendritic regions, because the temperature is closer to the melting temperature of the Ti-Fe phase. This leads to the formation of a homogenous Ti/Fe phase along the boundaries, as shown schematically in Figure 7(b). As the heat treatment progresses, Ti/W interdiffusion also occurs but at a slower rate. This leads to a relative enrichment in Fe in the boundary phase, driving the grain boundary phase into the C14 Laves phase region. This results in the observed formation of the TiFe2 C14 phase at grain boundaries and in precipitates. The Ti and Fe rich regions in the as-cast state are likely to be a liquid phase that formed an A2 structure during cooling, e.g. [2].

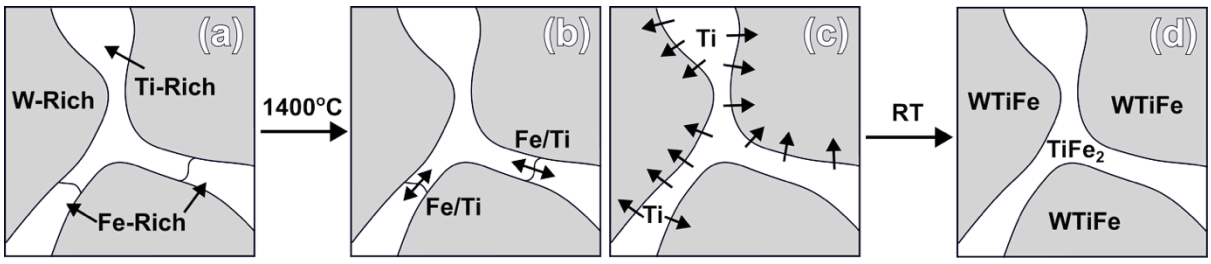

Figure 7: Schematic illustration showing the suggested mechanism for the formation of the C14 phase

Examination of the constituent phases suggests that the phase diagram shown in Figure 1 may overestimate the stability of the W_6Fe_7 μ phase relative to the C14 phase at 1400 ºC. To test this hypothesis, additional calculations were performed using Pandat to destabilise the μ phase at 1400 ˚C. The disagreement between the calculated isothermal section for the system and the measured compositions of the coexisting BCC and C14 phases has led to a remodelling of the μ-phase in the thermodynamic description for this system. Figure 8 shows the modified isothermal section of the W-Ti-Fe phase diagram at 1400 ˚C calculated using the improved model. Comparing this with Figure 1 shows that the size of the μ phase field decreases, and that a two-phase BCC + C14 phase region now exists. The experimentally measured compositions are also plotted and show a good agreement with the modified predictions. The earlier modelling of this system [36] relied on experimental data from the literature that was available for one temperature only (1000°C), making extrapolations to other

temperatures dangerous. Thus, the previous predictions shown in Figure 1 do not provide an accurate description of the high temperature stability of the C14 and μ phases, and the additional experimental data provided here enable an improved description of this system to be produced. The revised predictions shown in Figure 8 provide an improved preliminary prediction of the relative stabilities of the two phases.

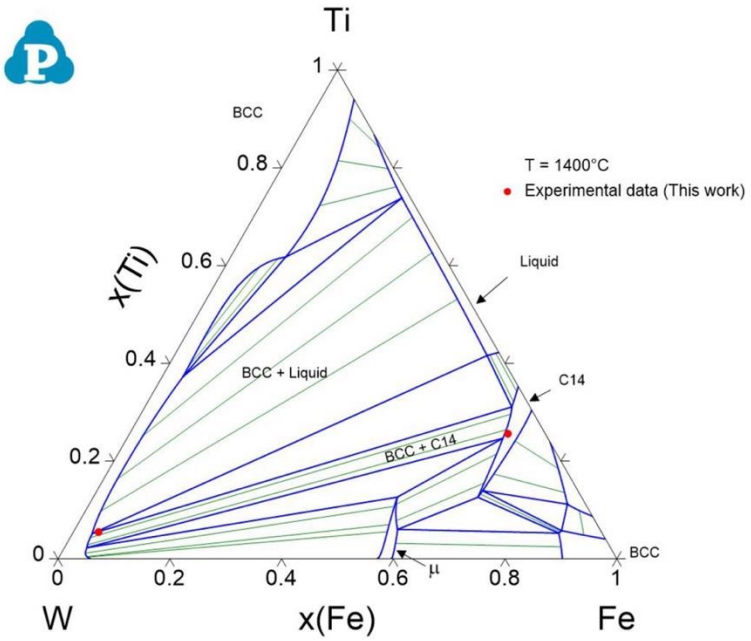

Figure 8: Revised 1400°C isothermal section of the W-Ti-Fe phase diagram showing concentrations in at.%. Experimental data shown in red corresponds to the experimentally measured compositions of the prior dendritic and prior inter-dendritic regions of the annealed specimen.

The average nanohardness as a function of depth from a 5x5 array of indents is shown in Figure 9(a). The indents were positioned across several of the A2 phase grains as shown in Figure 9(b). Some indents overlap the darker C14 phase at the grain boundaries but a significant variability in hardness across the indents is not observed. As shown these indents overlap with precipitates and the grain boundary phase. The average hardness at a depth of 1.5 μm was measured to be 6.25±0.07 GPa. As the plastic zone around the indent is approximately ten times greater than the indentation depth [31], this value represents the composite hardness of the C14-strenghtned matrix, but largely without any influence of grain boundary strengthening due to the large grain size. This is higher than comparable B2 reinforced WTiFe alloys [2], likely due to the low mobility of dislocations in the C14 phase observed with STEM and the incoherency of the matrix/precipitate phases limiting dislocation motion during deformation. Additionally dissolves Ti and Fe in the A2 W matrix may contribute towards solid solution strengthening, though it is noted that the concentration of Fe and Ti dissolved in the A2 phase is lower than was observed in previous iterations of this alloy . An average microhardness of 404 ± 29 $HV_{0.1}$ was measured from a total of 10 indents spaced across the specimen. This gives a higher hardness than previously reported W-Ti-Fe alloys tested in the solution-treated condition [1,2]. In these studies W-2.6Ti-0.2Fe (at.%) had a hardness of 370 HV_1 in the solution treated condition. After aging to induce the formation of a fine scale TiFe B2 phase the hardness increased to 514 HV_1. It is suggested that the significant hardening observed in this study is due primarily to the formation of the C14 phase.

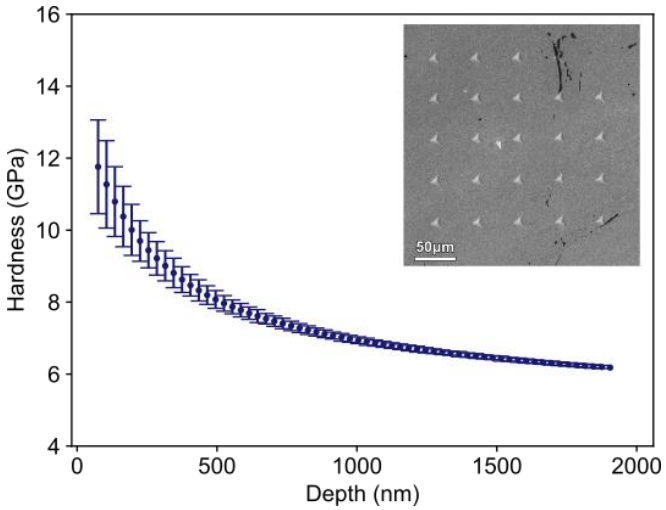

Figure 9: (a) Hardness vs depth data from the array of indents shown in the SE image in Figure 9(c), measured using CSM at a strain rate of 0.2 s^{-1}.

To investigate the relative hardness of the matrix and precipitate phase, an area was selected for mechanical property mapping. The selected area is shown in Figure 10and contains several different grains, (W,Ti)Fe_2 at the grain boundaries and a number of smaller isolated (W,Ti)Fe_2 precipitates. The shallow indents used for the mapping do not appear to show cracking, even in the hard Laves phase at the grain boundaries. No cracking was observed in secondary electron imaging of the deeper 2 um depth indents which measure the properties of both matrix and precipitate. Maps of hardness and modulus are shown in Figure 11 alongside quantitative EDS maps of the same region to highlight show the Laves phase.

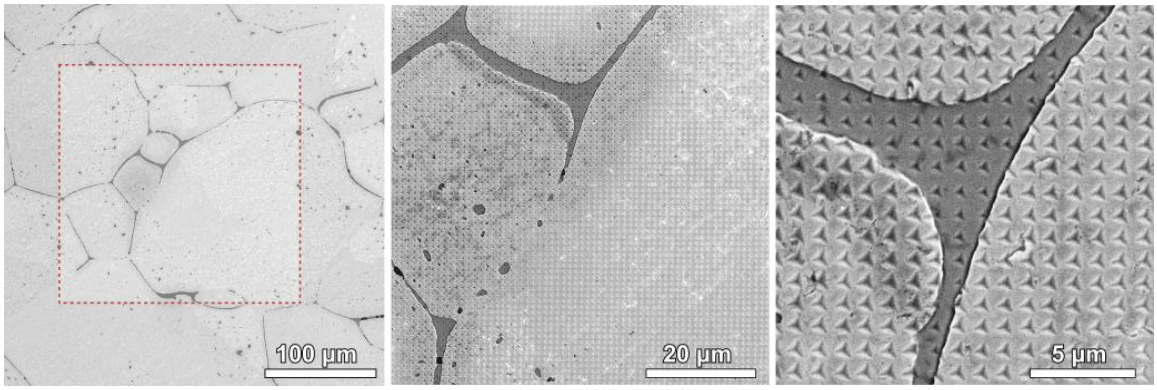

Figure 10: SE imaging showing the region mapped with the “NanoBlitz 3D” method

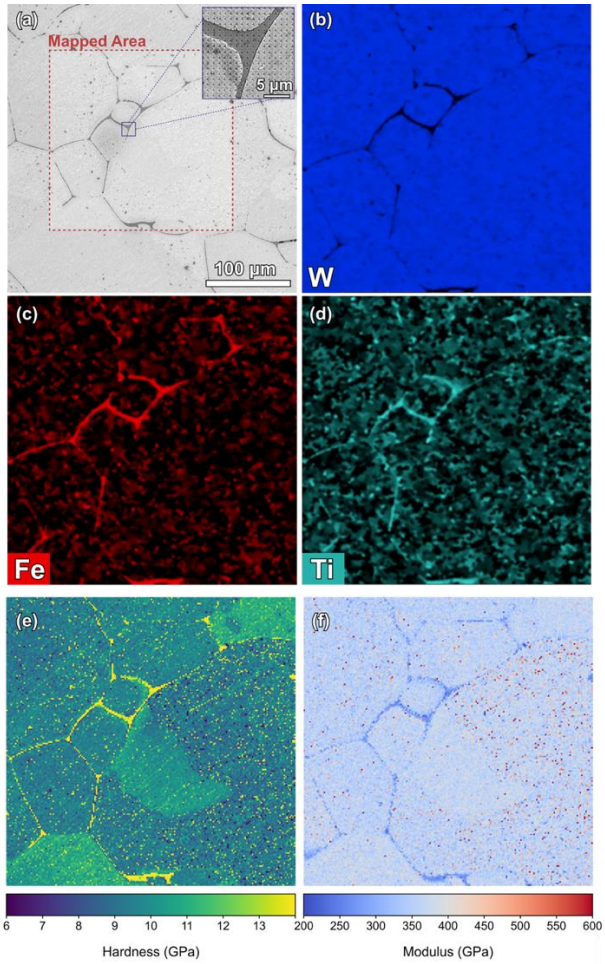

Figure 11: Correlated dataset from the same region: (a) secondary electron image, (b–d) quantitative EDS maps of W, Fe, and Ti concentrations, and (e–f) high-speed nanoindentation maps of hardness and elastic modulus (both in GPa).

The indentation hardness/modulus maps shown in Figure 11 suggest that the C14 Laves phase at the grain boundaries has a higher hardness and a lower modulus relative to the W-rich matrix. The hardness of the C14 phase was measured between 14 and 15 GPa compared with the hardness of the matrix phase which is between 7 and 12 GPa. The modulus of the C14 phase was on average around 250 GPa compared with around 400 GPa for the matrix phase. The shallow indents performed for mapping provide a qualitative assessment of the relative mechanical properties of the two phases but quantification of the hardness and modulus in these measurements are dominated by indentation size effects which cause a higher hardness at low indentation depths. Grain orientation appears to influence the hardness, with certain grains exhibiting a higher hardness in Figure 11. The hardness is considerably higher than the 2 um deep indents shown in Figure 9, which is due to the shallow indents used in the mapping method and the influence of indentation size effects [37]. There is also potential for strain rate effects to influence the results, as the rapid mapping technique operates at significantly higher loading rates compared to conventional nanoindentation, though in this instance we suggest that indentation size effects are the predominant cause of the higher hardness. The aim of the mapping technique is to provide a qualitative comparison between the phases to suggest what impact their formation will have on bulk mechanical properties.

Figure 12(a) shows a plot of the hardness vs the modulus in GPa for all 40,000 indentations, with a corresponding histogram of Figure 12(b) hardness and Figure 12(c) modulus. Further to the maps shown in Figure 11, the data plotted in Figure 12 shows a cluster of data with an average hardness of around 13.7 ± 2.2 GPa with an average modulus of around 367 ± 71 GPa, and a second larger set of data corresponding to the matrix, which has a lower average hardness and a higher modulus. The average hardness and modulus of each phase were

extracted from the data shown in Figure 12 (b) and (c) by fitting three Gaussian functions. The error reported on each average is the standard deviation of the data extracted from the curve fitting.

Generally, the modulus of a phase tends to increase with increasing hardness and the formation of Laves phase is usually expected to be detrimental to material properties. The ratio of H/E for the Laves phase is around 0.06. High hardness/low modulus Laves phases have been identified in ZrW magnetron sputtered films, but there is no available data on the mechanical properties of the $TiFe_2$ phase [38]. Ab-initio studies suggest that the $TiFe_2$ phase was comparatively brittle compared with other C14 phase materials such as $TiCr_2$ and $TiMn_2$, based on the calculated elastic modulus [35]. The low modulus of the $TiFe_2$ phase suggests that it can elastically deform at relatively low stress, but the high hardness measured suggests that it is resistant to plastic deformation. The modulus of the $TiFe_2$ phase predicted by DFT is also low compared with pure W, and some solid solution hardening is expected due to the dissolved Ti and Fe in the BCC matrix phase which could explain the low modulus. This can also be seen in Figure 10 where indents in the darker phase appear smaller, as the indenter tip has reached a shallower depth for a given load, due to the higher hardness.

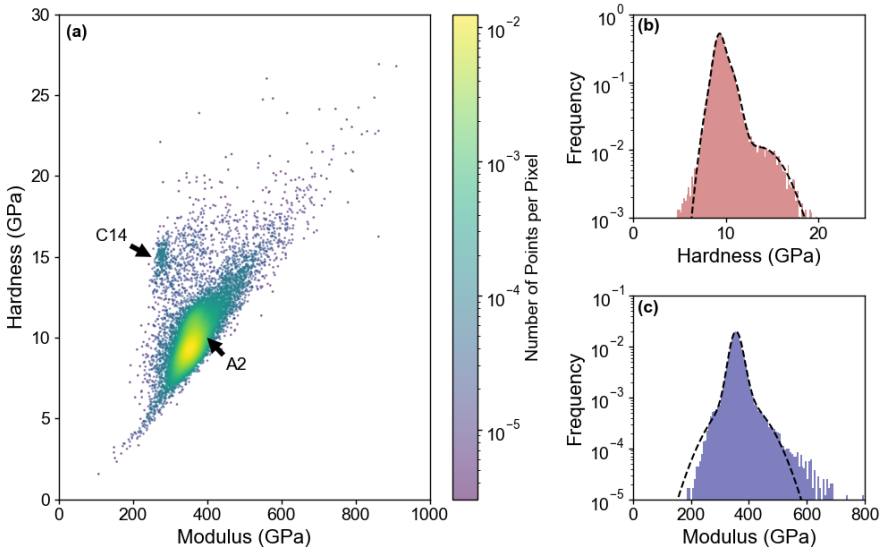

Figure 12: (a) Hardness vs Modulus data from nanoindentation mapping showing distinct regions associated with A2 and B2 phases, and histograms of (b) hardness and (c) modulus from indentation map

Conclusion

In this study, the phase stability and mechanical properties of a W-Ti-Fe alloy with $(W,Ti)Fe_2$ C14 Laves phase were investigated. Formation of the C14 phase was induced using a 72h heat treatment of a W-16%Ti-4%Fe (at.%) alloy at 1400°C. The annealing process resulted in the formation of a C14 secondary phase along the prior interdendritic boundaries and in smaller precipitates distributed across the specimen. The composition and crystal structure of the constituent phases were confirmed using SEM-EDS, STEM-EDS and diffraction pattern analysis, which showed the presence of the BCC-matrix and C14 $(W,Ti)Fe_2$ phase. The composition of the precipitate measured with SEM-EDS was 6.70±0.04%W, 25.64±0.18%Ti and 67.68±0.68%Fe (at.%), which was consistent with the STEM-EDS analysis. The ratio of Fe to Ti+W is also consistent with the C14 phase region of the ternary WTiFe phase diagram following $(W,Ti)Fe_2$. Nanoindentation showed that the specimen had a hardness of 6.25 GPa (nanoindentation) / 404 ± 29 $HV_{0.1}$ (microhardness), which is higher than comparable B2-strengthened WTiFe alloys. This is due to the formation of the C14 phase which acts as a strong barrier to dislocation motion, conferring high strength, but at risk of brittleness. High-speed, high-resolution nanoindentation mapping was used to show that the C14 phase along the boundaries had a hardness of 13.7 ± 2.2 GPa and a modulus of 367 ± 71 GPa. This hardness is high relative to the BCC W matrix which had a hardness of 9.7 ± 1 GPa. This study has led to an improved understanding of phase stability in W-rich W-Ti-Fe alloys and has helped to develop a refinement of the existing phase diagram.

Acknowledgements

M. Lloyd acknowledges support from the UKRI National Nuclear User Facility through Experiment 222 (awarded under NNUF Larger Projects Competition 2023), “Proton Irradiation and Micro-mechanical Testing of Refractory Alloys.” The research used UKAEA's Materials Research Facility, which has been funded by and is part of the UK's National Nuclear User Facility and Henry Royce Institute for Advanced Materials. A. J. Knowles acknowledges support from: UKRI Future Leaders Fellowship (MR/T019174/1 & MR/Y034155/1) and Royal Academy of Engineering Research Fellowship (RF\201819\18\158).

CREDIT statement

References

[1] N. Parkes, R. Dodds, A. Watson, D. Dye, C. Hardie, S.A. Humphry-Baker, A.J. Knowles, Int J Refract Metals Hard Mater 113 (2023) 106209.

[2] A.J. Knowles, D. Dye, R.J. Dodds, A. Watson, C.D. Hardie, S.A. Humphry-Baker, Appl Mater Today 23 (2021) 101014.

[3] S. Huang, Y. Gao, K. An, L. Zheng, W. Wu, Z. Teng, P.K. Liaw, Acta Mater 83 (2015) 137–148.

[4] A.J. Knowles, T.-S. Jun, A. Bhowmik, N.G. Jones, T. Ben Britton, F. Giuliani, H.J. Stone, D. Dye, Scr Mater 140 (2017) 71–75.

[5] S.A. Kube, C. Frey, C. McMullin, B. Neuman, K.M. Mullin, T.M. Pollock, Acta Mater 265 (2024) 119628.

[6] K. Ma, T. Blackburn, J.P. Magnussen, M. Kerbstadt, P.A. Ferreirós, T. Pinomaa, C. Hofer, D.G. Hopkinson, S.J. Day, P.A.J. Bagot, M.P. Moody, M.C. Galetz, A.J. Knowles, Acta Mater 257 (2023) 119183.

[7] E. Gaganidze, A. Chauhan, H.C. Schneider, D. Terentyev, G. Borghmans, J. Aktaa, Journal of Nuclear Materials 547 (2021) 152761.

[8] E. Gaganidze, A. Chauhan, H.C. Schneider, D. Terentyev, B. Rossaert, J. Aktaa, Journal of Nuclear Materials 556 (2021) 153200.

[9] D. Terentyev, C. Yin, A. Dubinko, C.C. Chang, J.H. You, Int J Refract Metals Hard Mater 95 (2021) 105437.

[10] Y. Kim, K.H. Lee, E.P. Kim, D.I. Cheong, S.H. Hong, Int J Refract Metals Hard Mater 27 (2009) 842–846.

[11] C. Yin, D. Terentyev, T. Pardoen, A. Bakaeva, R. Petrov, S. Antusch, M. Rieth, M. Vilémová, J. Matějíček, T. Zhang, Int J Refract Metals Hard Mater 75 (2018) 153–162.

[12] A.A.N. Németh, J. Reiser, D.E.J. Armstrong, M. Rieth, Int J Refract Metals Hard Mater 50 (2015) 9–15.

[13] O. El-Atwani, J.A. Hinks, G. Greaves, S. Gonderman, T. Qiu, M. Efe, J.P. Allain, Scientific Reports 2014 4:1 4 (2014) 1–7.

[14] O. El-Atwani, S. Gonderman, M. Efe, G. De Temmerman, T. Morgan, K. Bystrov, D. Klenosky, T. Qiu, J.P. Allain, Nuclear Fusion 54 (2014) 083013.

[15] L. Tan, T. Graening, X. Hu, W. Zhong, Y. Yang, S.J. Zinkle, Y. Katoh, Journal of Nuclear Materials 540 (2020) 152376.

[16] Y. Kitsunai, H. Kurishita, H. Kayano, Y. Hiraoka, T. Igarashi, T. Takida, Journal of Nuclear Materials 271–272 (1999) 423–428.

[17] S. Lang, Q. Yan, N. Sun, X. Zhang, L. Deng, Y. Wang, C. Ge, J Alloys Compd 660 (2016) 184–192.

[18] S. Novak, M. Kocen, A. Šestan Zavašnik, A. Galatanu, M. Galatanu, S. Tarancón, E. Tejado, J.Y. Pastor, P. Jenuš, Materials Science and Engineering: A 772 (2020) 138666.

[19] D. Terentyev, P. Jenus, E. Sal, A. Zinovev, C.C. Chang, C. Garcia-Rosales, M. Kocen, S. Novak, W. Van Renterghem, Nuclear Fusion 62 (2022) 086035.

[20] K. Ma, P.A. Ferreirós, T.W. Pfeifer, R.G. Abernethy, S. von Tiedemann, N. Peng, G. Greaves, C. Ophus, K. Sun, A.H. Mir, L. Wang, S. Huang, S. Zhao, P.E. Hopkins, C.D. Hardie, A.J. Knowles, Acta Mater (2025) 121095.

[21] A.J. Knowles, A. Bhowmik, S. Purkayastha, N.G. Jones, F. Giuliani, W.J. Clegg, D. Dye, H.J. Stone, Scr Mater 140 (2017) 59–62.

[22] N. Saunders, A.P. Miodownik, CALPHAD Calculation of Phase Diagrams: A Comprehensive Guide, Elsevier, 1998.

[23] H. Lukas, S.G. Fries, B. Sundmanm, Computational Thermodynamics: The CALPHAD Method, Cambridge University Press, 2007.

[24] X. Xiao, M. Jin, W. Qin, J. Yao, High Temperature Materials and Processes 43 (2024).

[25] A. Von Keitz, G. Sauthoff, Intermetallics (Barking) 10 (2002) 497–510.

[26] C.D. Rabadia, Y.J. Liu, L.Y. Chen, S.F. Jawed, L.Q. Wang, H. Sun, L.C. Zhang, Mater Des 179 (2019) 107891.

[27] L. Sun, T.H. Simm, T.L. Martin, S. McAdam, D.R. Galvin, K.M. Perkins, P.A.J. Bagot, M.P. Moody, S.W. Ooi, P. Hill, M.J. Rawson, H.K.D.H. Bhadeshia, Acta Mater 149 (2018) 285–301.

[28] A. Bhowmik, H.J. Stone, Metallurgical and Materials Transactions A 43 (2012) 3283–3292.

[29] L.A. Giannuzzi, F.A. Stevie, Micron 30 (1999) 197–204.

[30] W.C. Oliver, G.M. Pharr, J Mater Res 7 (1992) 1564–1583.

[31] J. Chen, S.J. Bull, Surf Coat Technol 201 (2006) 4289–4293.

[32] W.D. Nix, H. Gao, J Mech Phys Solids 46 (1998) 411–425.

[33] NanoBlitz 3D Mechanical Property Mapping User Instructions, (SKYD-1252-0), Nanomechanics, Inc., n.d.

[34] F.R. de Boer, W.C.M. Mattens, R. Boom, A.R. Miedema, A.K. Niessen, Cohesion in Metals. Transition Metal Alloys, North-Holland ; Sole distributors for the U.S.A. and Canada, Elsevier Scientific Pub. Co, Amsterdam ; New York : New York, N.Y., U.S.A., 1988.

[35] Z.S. Nong, J.C. Zhu, Y. Cao, X.W. Yang, Z.H. Lai, Y. Liu, Physica B Condens Matter 419 (2013) 11–18.

[36] C. Qiu, Z. Jin, Scripta Metallurgica et Materialia 28 (1993) 85–90.

[37] Z. Shen, Y. Su, Z. Liang, X. Long, Journal of Materials Research and Technology 31 (2024) 117–132.

[38] D. Horwat, E. Jimenez-Pique, J.F. Pierson, S. Migot, M. Dehmas, M. Anglada, Journal of Physics and Chemistry of Solids 73 (2012) 554–558.